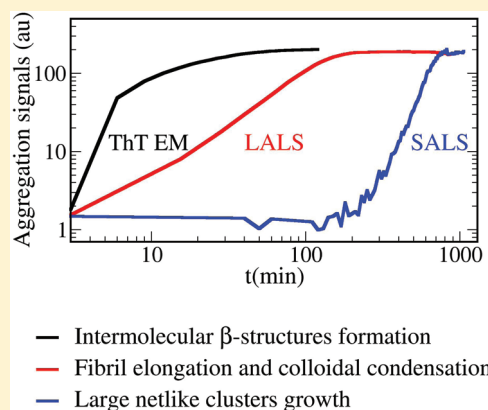


## Amyloid Fibrils Formation of Concanavalin A at Basic pH

R. Carrotta,<sup>\*,†</sup> V. Vetri,<sup>†,‡</sup> F. Librizzi,<sup>‡</sup> V. Martorana,<sup>†</sup> V. Militello,<sup>†,‡</sup> and M. Leone<sup>†,‡</sup><sup>†</sup>Istituto di Biofisica, Consiglio Nazionale delle Ricerche, Via Ugo La Malfa 153, 90146 Palermo, Italy<sup>‡</sup>Dipartimento di Scienze Fisiche e Astronomiche, Università di Palermo, Via Archirafi 36, 90123 Palermo, Italy

**ABSTRACT:** Mechanisms of partial unfolding and aggregation of proteins are of extreme interest in view of the fact that several human pathologies are characterized by the formation and deposition of protein-insoluble material, mainly composed of amyloid fibrils. Here we report on an experimental study on the heat-induced aggregation mechanisms, at basic pH, of concanavalin A (ConA), used as a model system. Thioflavin T (ThT) fluorescence and multiangle light scattering allowed us to detect different intertwined steps in the formation of ConA aggregates. In particular, the ThT fluorescence increase, observed in the first phase of aggregation, reveals the formation of intermolecular  $\beta$ -sheet structure which constitutes a rate-limiting step of the process. The intertwining between the formation of  $\beta$ -aggregate structures and the whole aggregation process is discussed as a function of protein concentration: a coagulation process produces the same kind of aggregates at the different concentrations studied. Multiangle light-scattering data highlight the onset of the condensation process which gives rise to formation of compact fractal aggregates. AFM microscopy supports this conclusion showing thin fibrils of ConA, formed in the early stage of aggregation, which further interact to form larger structures with a netlike spatial organization.



## ■ INTRODUCTION

Understanding of protein aggregation is a fundamental target in many research areas, from physics to medicine, and from biotechnology to pharmaceutical industry. Many human protein disorders are correlated with formation of proteinaceous deposits, often containing ordered aggregates, called amyloid fibrils.<sup>1</sup> Amyloid fibrils formation can be characterized by selected experimental features, such as green birefringence upon staining with Congo Red dye, fluorescence emission of the Thioflavin T dye, increase of  $\beta$ -sheet secondary structure content with respect to the native protein as detected by infrared absorption and/or circular dichroism spectroscopy, and typical fibrillar morphology seen by microscopy techniques.<sup>2</sup> In vitro studies of different model proteins involved or not in pathological events showed up the ability of any polypeptide chain to aggregate forming fibrils, under suitable conditions.<sup>3</sup> The amyloid final structure is characterized by high stability and difficulty to be dissolved back to the native state. In the past decades, it has become evident the major role played by destabilizing conditions (choice of pH, increase of temperature, addition of cosolvents, sequence mutations) in prompting amyloid aggregation mechanisms, to favor both intermolecular interactions and partially unfolded protein states prone to associate.<sup>4–6</sup> The presence of common structural features in amyloid fibrils, no matter which protein they are made of, suggests that in the process to find the highly stable amyloid superstructure rich in intermolecular  $\beta$  structures, conformational changes at the level of tertiary and secondary structure are strongly implicated.<sup>7,8</sup>

Light scattering is a widely used technique to monitor protein stability and protein coagulation processes, as well as liquid–

liquid phase transitions and crystallization regimes.<sup>5,9–11</sup> Time course static light scattering from an aggregating solution gives an estimate of the weight-averaged molecular mass growth during the process. Simultaneous time course dynamic light scattering allows following also the growth of the average hydrodynamic radius of the aggregates in solution. Moreover, time evolution of the solution structure factor adds information about the aggregates' structural properties.<sup>12,14</sup>

Thioflavin T (ThT) is one of the most used dyes for detection and kinetic characterization in amyloid fibrils formation. Under binding to amyloid structures, ThT fluorescence properties specifically change.<sup>15</sup> A few studies, focusing on structural modeling, try to explain the specific fluorescence coming from ThT bound to fibrils.<sup>16–19</sup> Major points are the presence and the accessibility of cavities or surfaces where ThT can bind. While ThT emission is related to conformational properties of the aggregates, light scattering is sensitive to the average mass and the hydrodynamic size and shape of the solute molecules. The combination of the two methods is a very useful tool to highlight different features of amyloid growth.

Concanavalin A (ConA) is a 26 kDa lectin protein, extracted from jack bean and constituted by 237 amino acid residues.<sup>20</sup> Above pH 7, the protein quaternary structure is characterized by a tetramer, made of two identical dimers, perpendicularly arranged. Each monomer presents 12  $\beta$ -sheets organized in a

Received: May 10, 2010

Revised: January 12, 2011

Published: March 10, 2011

jellyroll motif.<sup>21</sup> ConA shows a large structural homology to the human serum amyloid protein, SAP,<sup>22</sup> a two-pentameric subunits protein, which binds to all forms of amyloid fibrils and is generally present in all the in vivo fibrillar deposits. ConA aggregation has been studied as a function of pH, showing the occurrence of two different pathways leading to the formation of amyloids or amorphous aggregates. The relative weight of these two pathways is modulated by pH: amorphous aggregates are preferentially formed at low pH values, while fibrils formation is favored at high pH values.<sup>23</sup> Interestingly, by means of simultaneous CD and ThT fluorescence measurements, we have found that a strict correlation between ThT binding and changes at the secondary structure level exists.<sup>23,32</sup> The time evolution of these signals was also found to parallel 8-anilino-1-naphthalenesulfonate (ANS) fluorescence increase, probing the formation of new hydrophobic regions during the evolution of the aggregation process.

To focus on the mechanisms of fibril formation, in the present study the ConA aggregation process at basic pH (pH 8.9) and  $T = 37^\circ\text{C}$  has been monitored at different protein concentrations by dynamic and multiangle static light scattering and by in situ ThT fluorescence emission measurements. Overall, the results allowed to describe different mechanisms involved in ConA aggregation from the initial formation of thin fibrils to the growth of larger fractal aggregates, in longer time scale, due to the association of preformed ConA aggregates.

## EXPERIMENTAL METHODS

**Sample Preparation.** ConA (type IV, L7647) and ThT were purchased from Sigma Aldrich and used without further purification. All the measurements were performed in phosphate buffer 0.1 M pH 8.9. Protein concentration was determined by UV absorption at  $\lambda = 280\text{ nm}$ , using  $\varepsilon = 33\,280\text{ cm}^{-1}\text{ M}^{-1}$  and ranged from about 0.1 to 1.4 mg/mL. Each solution was freshly prepared at  $6^\circ\text{C}$  and filtered just before the measurement through  $0.22\text{ }\mu\text{m}$  filters.

**ThT Fluorescence.** ConA aggregation was studied by monitoring in situ ThT binding from solutions incubated at  $T = 37^\circ\text{C}$ . ThT final concentration in ConA solutions was  $13.3\text{ }\mu\text{g/mL}$ . ThT did not change the ConA aggregation process, as checked by monitoring time course turbidity from the aggregating solution, with and without dye. Emission spectra were measured using a Jasco FP-6500 instrument equipped with a Jasco ETC-273T Peltier as temperature controller. Samples were filtered in a 1 cm path cuvette and, after 3 min for thermal equilibration, emission spectra were recorded ( $\lambda_{\text{ex}} = 440\text{ nm}$ , emission and excitation bandwidth 3 nm, scan speed  $100\text{ nm/min}$ , integration time 1 s). It was verified that hydroxylation processes at basic pH did not affect fibril detection.<sup>24</sup>

**Static and Dynamic Light Scattering (SLS and DLS).** Time-resolved light scattering experiments were carried on solutions incubated at  $T = 37^\circ\text{C}$ , immediately after ConA dissolution in 0.1 M phosphate buffer pH 8.9 and direct filtration in cuvette. The cuvette was placed in a thermostatically controlled cell compartment of a Brookhaven Instrument BI200-SM goniometer, equipped with a 100 mW solid-state laser at  $\lambda_0 = 532\text{ nm}$ . Temperature was controlled by a circulating bath with a tolerance within  $0.05^\circ\text{C}$ . Scattered light intensity at  $90^\circ$  ( $q = 23\text{ }\mu\text{m}^{-1}$ ),  $I_{90^\circ}(t)$ , and its time autocorrelation function,  $g_2(t)$ , were measured simultaneously by using a Brookhaven BI-9000 correlator. The static scattered light was monitored in order to follow

the growth of the weight-averaged mass  $M_w$  in the aggregation process of the protein, according to the fact that

$$I_{90^\circ} \propto k c M_w P(\theta = 90^\circ) \quad (1)$$

with  $P$  representing the form factor and  $k = [(4\pi^2 n^2)/(\lambda_0^4 N_A)](dn/dc)^2$ , where  $n$  is the refraction index of the solution at  $T = 37^\circ\text{C}$ ,  $N_A$  is the Avogadro number,  $\lambda_0$  is the in vacuo laser wavelength,  $dn/dc$  is the derivative of  $n$  with respect to the protein concentration (we consider  $dn/dc = 0.18\text{ cm}^3\text{ g}^{-1}$ ), and  $c$  is the protein concentration.<sup>12</sup>  $P(90^\circ) \leq 1$ . The decrease in intensity is due to the increase of the scatterer's average size,  $d$  ( $d \geq \lambda_0/10$ ). The low-concentration regime ( $c \leq 1.4\text{ mg/mL}$ ) allows neglecting structure effects due to protein interactions. Time-resolved light scattering for the solution at  $c = 0.55\text{ mg/mL}$  was monitored as a function of the scattering vector  $q$ , in the range  $5\text{--}30\text{ }\mu\text{m}^{-1}$  (large-angle light scattering) in order to obtain the time evolution of the form factor  $P(q)$ . Field autocorrelation functions  $g_1(t)$  at  $90^\circ$ , obtained from

$$g_2(t) = 1 + B g_1^2(t) \quad (2)$$

with  $B < 1$ , were analyzed using a smoothing constrained regularization method,<sup>25</sup> in order to obtain the distribution  $P(D)$  of the apparent diffusion coefficients  $D$

$$g_2(t) = 1 + B \left| \int P(D) e^{-Dq^2 t} dD \right|^2 \quad (3)$$

where  $B$  is a factor accounting for the experimental setup (ideally  $B = 1$ ),  $q$  is the scattering vector defined as  $q = [(4\pi n)/\lambda_0] \sin(\theta)/2$ , with  $n$  the medium refractive index at  $T = 37^\circ\text{C}$  and  $\theta$  the scattering angle. We can express the apparent diffusion coefficient as a function of the  $z$ -averaged hydrodynamic radius  $R_h$  by using the Stokes–Einstein relation

$$D = \frac{KT}{6\pi\eta R_h} \quad (4)$$

where  $k$  is the Boltzmann constant,  $T$  the absolute temperature, and  $\eta$  the solvent viscosity. Thus, we obtain the distribution  $P(R_h)$  of the  $z$ -averaged hydrodynamic radius. The harmonic mean of the hydrodynamic radius is calculated from the mean value of the distribution  $P(D)$ :

$$\langle R_h \rangle_{\text{harm}} = \frac{KT}{6\pi\eta\langle D \rangle} = \frac{KT}{6\pi\eta} \left( \int P(D) D dD \right)^{-1} \quad (5)$$

Absolute scale for the scattered intensity was obtained by normalization with respect to toluene, whose Rayleigh ratio at  $532\text{ nm}$  was taken as  $28 \times 10^{-6}\text{ cm}^{-1}$ .

**Small-Angle Light Scattering (SALS).** For the samples at  $c = 0.12, 0.55$ , and  $0.86\text{ mg/mL}$ , time-resolved light scattering was measured as a function of the scattering wave vector  $q$ , spanning the range  $0.02\text{--}2\text{ }\mu\text{m}^{-1}$ , by using a homemade experimental setup<sup>26</sup> equipped with a 20 mW helium–neon laser and a charged coupled device Pulnix TM765 camera. Measurable intensities can span a wide dynamical range (from 1 to  $33\,105\text{ au}$ ) due to a software integration of multiple exposure times ( $1/60$  to  $1/10\,000\text{ s}$ ). SALS data are not in absolute scale and therefore to join LALS and SALS data, low  $q$  data were scaled to the high  $q$  ones by assuming that lower  $q$  SALS data lie on the straight line (in log–log scale) determined by fitting the high  $q$  LALS data. This was done by using the structure factor measured after 320 min of incubation at  $T = 37^\circ\text{C}$ . The scaling factor for LALS data was then applied to all sets of data, observing a general

good agreement. The analysis of the structure factor data has been performed by assuming a fractal model for the aggregate. We used the expression

$$S_m(q) = \frac{1}{m} \left[ 1 + \frac{d_f \Gamma(d_f - 1) \sin((d_f - 1) \arctan(q\xi))}{(qr_0)^{d_f} \left( 1 + \frac{1}{q^2 \xi^2} \right)^{(d_f - 1)/2}} \right] \quad (6)$$

for  $qr_0 < 1 < q\xi^{1/2}$

where  $m$  is the number of identical building units of radius  $r_0$  in the aggregate,  $\Gamma$  is the gamma function,  $\xi$  gives indication of the cluster size, and  $d_f$  is the fractal dimension, related to the structural packing of the fractal cluster. The function used is obtained analytically by assuming an exponential cutoff function, with the exponent  $\xi$  giving the size of the fractal aggregate. Late-stage structure factors were fit by also considering a hard-sphere interaction between the fractal clusters ( $I(q) = S_m(q)S_{hs}(q, D/2, \phi)$ ), whose fit parameters,  $D/2$  and  $\phi$ , give the hard-sphere radius and volume fraction respectively.

**AFM Measurements.** ConA solution (0.5 mg/mL), incubated at 37 °C for about 400 min, was diluted 50 times in bidistilled demineralised water and small aliquots (10  $\mu$ L) were deposited on freshly cleaved mica. The samples were dried by a gentle nitrogen flux and imaged in air. AFM images were acquired in different regions of each sample in tapping mode using a Veeco Multimode Nanoscope V workstation (Santa Barbara, CA). Etched-silicon probes with a pyramidal-shape tip having a nominal curvature of 8 nm and a nominal internal angle of 25° were used for imaging. The drive frequency was around 300 kHz and the scan rate was between 0.5 and 0.8 Hz. Height and phase images were collected by capturing 512  $\times$  512 points in each scan.

## RESULTS

In order to study the mechanism of fibrils formation in solutions of ConA at basic pH, experiments at different protein concentrations have been performed at  $T = 37$  °C.

It has been reported that ConA undergoes conformational changes and aggregation in the pH range above 8, with a parallel loss of sugar binding activity.<sup>27–30</sup> However, the instability of ConA at high pH values only recently has been related to amyloid fibril formation.<sup>23,31,33</sup>

The dimer–tetramer equilibrium is dependent on pH. Below pH 5 (the protein isoelectric point) ConA is a dimer, while for higher values of pH is mainly a tetramer. After dissolution in potassium phosphate buffer at pH 8.9, protein aggregation starts almost immediately as shown by light-scattering results reported later in this section. ConA in its native state, similarly to other all- $\beta$  native proteins like  $\beta$ -lactoglobulin,<sup>32</sup> does not strongly interact with ThT. In these conditions and at 37 °C, we observe the progressive increase of ThT fluorescence that in turn indicates the formation of binding regions for this dye. The time course of in situ Thioflavin T fluorescence measurements at five different protein concentrations is reported in Figure 1a. Continuous lines represent data fits according to the empirical stretched exponential function  $A(1 - e^{-(t/\tau)^\beta})$ , with a constant exponent  $\beta = 0.7$ . The analysis aims at extracting a characteristic time of the ThT binding process ( $\tau$ ) as a function of the concentration. However,

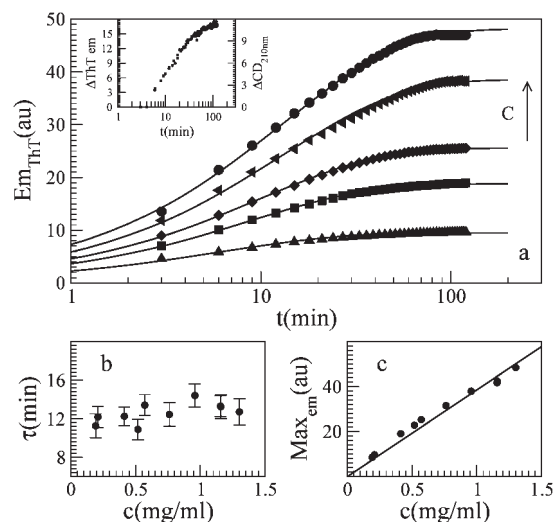


**Figure 1.** ThT emission at  $\lambda = 484$  nm at different protein concentration (0.2, 0.41, 0.57, 0.96, 3 mg/mL) (a). The lines represent the fitting curves according to an exponential stretched function. In the inset,  $CD_{210\text{ nm}}$  ( $\bullet$ , 0.5 mg/mL) and ThT emission ( $\blacksquare$ , 0.57 mg/mL) increments are reported. Characteristic time (b) and plateau value (c) obtained by the data analysis.

we wish to note that this behavior is the fingerprint of the complexity of the observed process, arising from conformational and/or dynamical heterogeneity in the formation of  $\beta$ -aggregate structure. Indeed, stretched exponential function usually describes phenomena characterized by the presence of a highly heterogeneous sequence of events resulting from a distribution of energy barriers.

Figure 1 reports also the parameter  $\tau$  (panel b) and the plateau value (panel c) as a function of concentration. ThT binding rate is independent of concentration (Figure 1b) while the final value of ThT fluorescence intensity is proportional to the concentration (Figure 1c). This clearly indicates that the concentration of aggregate structures that bind ThT (or better of binding sites for this dye) depends only on native protein concentration. In a previous study on the early stages of ConA aggregation process at pH 8.9, it was shown that amyloid formation is triggered by the transition to a partially unfolded structure; ThT emission increase was found to occur simultaneously with secondary structures changes seen by CD.<sup>23</sup> In particular, the CD absorption (at  $\lambda = 210$  nm) follows the same trend as ThT fluorescence and the two kinetics showed a time dependence which can be described in terms of stretched exponential. We show in the inset of Figure 1a the correlation between the time evolution CD intensity and ThT intensity at pH 9 and 37 °C. These data confirm what has been previously observed at a slightly higher temperature ( $T = 40$  °C).<sup>23</sup> The intensity decrease in the CD spectrum at  $\lambda = 210$  nm is detected in many cases of amyloid fibril aggregation and is related to the formation of intermolecular  $\beta$ -structure in ordered aggregates. The agreement of the ThT binding data with the CD data<sup>23</sup> indicates that ThT fluorescence accounts for the gradual formation of  $\beta$ -aggregate structures, as suggested also by Krebs et al. (2008).<sup>34</sup> Moreover, FTIR measurements on ConA aggregates, grown in analogous conditions, have shown the presence of  $\beta$ -sheets aggregates with strong intermolecular hydrogen bonds (usually found in amyloid structures), and of a little amount of antiparallel intermolecular  $\beta$ -sheets.<sup>33</sup>



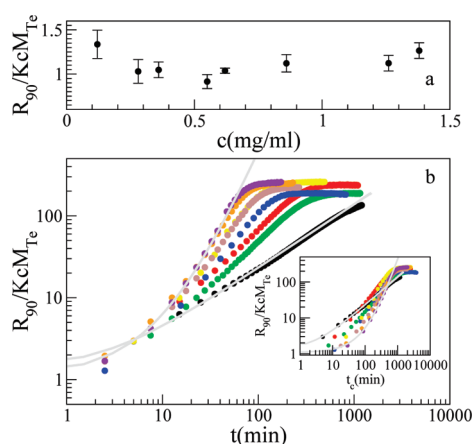
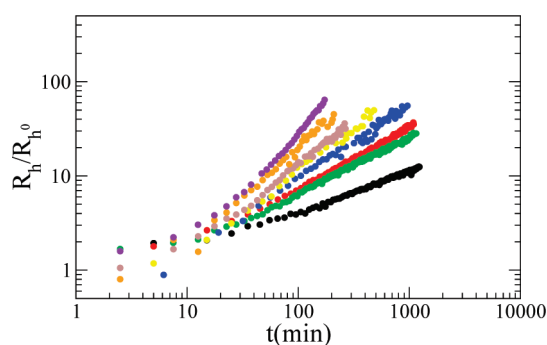


**Figure 2.** Weight-averaged molecular mass normalized to the ConA tetramer mass (aggregation number), obtained by measuring the Rayleigh ratio at the beginning of the incubation at  $T = 37^\circ\text{C}$ , for solutions at different protein concentration (a). Time course of the Rayleigh ratio normalized to the tetramer scattering at different protein concentrations (0.12 mg/mL, black; 0.28 mg/mL, red; 0.36 mg/mL, green; 0.55 mg/mL, blue; 0.62 mg/mL, yellow; 0.86 mg/mL, brown; 1.26 mg/mL, orange; 1.38 mg/mL, violet) (b). The gray lines represent the fitting curves according to a colloid model with homogeneous kernel (see expression 7 in the Discussion section). In the inset, the time axis has been scaled with the transformation  $t_c = t(c/c_0)$ , where  $c_0 = 0.12$  mg/mL.

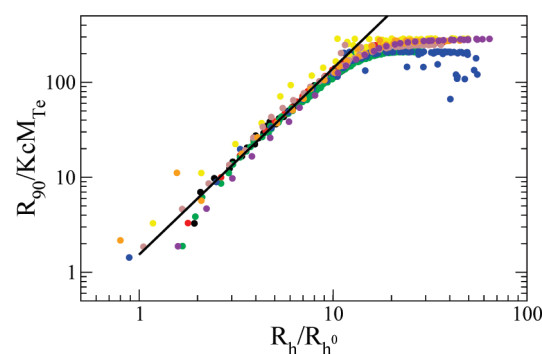
ConA aggregation has been also monitored by static and dynamic light scattering at different concentrations with the aim of understanding the pathway leading to aggregates formation. The Rayleigh ratio at  $q = 23\ \mu\text{m}^{-1}$  ( $\theta = 90^\circ$ ), normalized in order to obtain the weight-averaged molar mass of the protein, was read immediately after incubation at  $T = 37^\circ\text{C}$ , and the results are reported in Figure 2a, divided by the theoretical tetramer molecular mass. Although the ConA instability under these conditions makes it difficult a mass evaluation, the results in Figure 2a indicate that, at the beginning of the aggregation process, this protein is mainly in the tetrameric form at all the concentrations investigated.

Figure 2b reports on the time evolution of the Rayleigh ratio measured at  $q = 23\ \mu\text{m}^{-1}$  (normalized to the Rayleigh ratio calculated for a tetramer) for samples with different concentrations, incubated at  $T = 37^\circ\text{C}$ . The growth of the scattering intensity indicates that the protein molecules associate, forming higher molecular mass scatterers. The process starts with a tetramer and an immediate monotonic growth is detected at all the concentrations leading to a plateau. We remark here that the aggregation rate monitored by the Rayleigh ratio reported in Figure 2b does depend on concentration while the characteristic time  $\tau$  extracted by ThT binding experiments does not. In order to gain insight on the concentration dependence of the Rayleigh ratio growth rate, we replicated the plot in Figure 2b by scaling the time axis for the concentration ( $t_c = t(c/c_0)$ ) in the inset of Figure 2b). The overall poor scaling and the fact that high concentration data lay behind in the early stage of the kinetics point to a sublinear concentration dependence of the initial rate. This can be explained by the effect of a concentration-independent rate-limiting step signaled by the ThT fluorescence data.

Simultaneously to the static intensity, also time evolution of the intensity autocorrelation functions is monitored. The average hydrodynamic radius is extracted by the analysis of the intensity



**Figure 3.** Growth of the hydrodynamic radius, normalized to the initial value (ConA tetramer  $R_h^0$ ). The different colors correspond to different protein concentrations (0.12 mg/mL, black; 0.28 mg/mL, red; 0.36 mg/mL, green; 0.55 mg/mL, blue; 0.62 mg/mL, yellow; 0.86 mg/mL, brown; 1.26 mg/mL, orange; 1.38 mg/mL, violet).



**Figure 4.** Log–log plot of the Rayleigh ratio, normalized to the tetramer scattering, versus the hydrodynamic radius, normalized to the initial value  $R_h^0$ , at different protein concentrations (0.12 mg/mL, black; 0.28 mg/mL, red; 0.36 mg/mL, green; 0.55 mg/mL, blue; 0.62 mg/mL, yellow; 0.86 mg/mL, brown; 1.26 mg/mL, orange; 1.38 mg/mL, violet). The line represents a power law with exponent 2.

autocorrelation function (as reported in the Experimental Methods section) at different times. Figure 3 shows that the average hydrodynamic radius normalized to the initial tetramer value  $R_h^0 = 5\ \text{nm}$  grows monotonically even when the scattering intensity shows the tendency to reach a plateau. This behavior can be explained considering that at  $90^\circ$  ( $q = 23\ \mu\text{m}^{-1}$ ) the aggregates larger than about 50 nm produce a significantly lower scattering intensity signal, due to the form factor effects. Consequently, as the aggregates size reaches a critical dimension (of the order of a micrometer) the detection method may become even insensitive to such species. On the other hand, the intensity autocorrelation function can still detect these larger species, although with a low signal-to-noise ratio.

Figure 4 shows for all the concentrations studied the correlation between the normalized Rayleigh ratio and the hydrodynamic radius normalized to the tetramer radius in a log–log plot, in order to have indication of the structural properties of the aggregates forming in the early stage of the process. Data overlap indicates that the same kind of aggregates form at all the concentrations studied. For species with hydrodynamic radius below 50 nm ( $R_h/R_h^0 < 10$ ) no form factor correction is required and data can be fitted with a power law, according to the expression  $M_{\text{ag}}/M_{\text{Te}} = [R_h/R_h^0]^\alpha$  with  $\alpha = 2$ . A power law with  $\alpha = 2$  well approximates the expression found in the case of

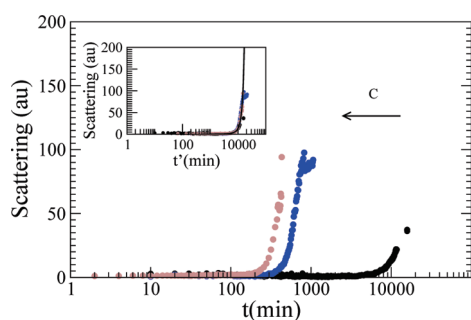


**Figure 5.** Small-angle light scattering measured at  $q = 0.42 \mu\text{m}^{-1}$ , for three different protein concentrations (0.12 mg/mL, black; 0.55 mg/mL, blue; 0.86 mg/mL, brown). In the inset, the data sets at higher concentrations have been scaled (by scaling the time axis with the concentration) on top to the lowest concentration data set and the line represents a fitting curve according to an exponential function.

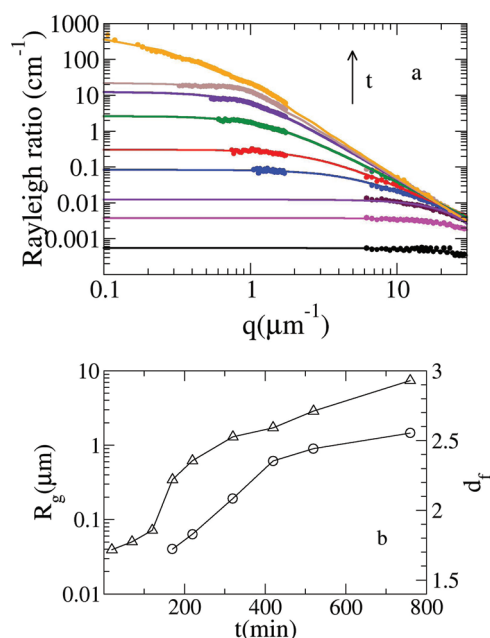


**Figure 6.** Time course structure factors for  $c = 0.55 \text{ mg/mL}$ . A few representative data sets at different incubation times (20 min, black; 70 min, magenta; 120 min, maroon; 170 min, blue; 220 min, red; 320 min, green; 420 min, violet; 520 min, brown; 760 min, orange) (a). The lines represent the fitting curves according to the Guinier model (20, 70, and 120 min), the fractal model (170, 220, 320, and 420 min), and the fractal model with a hard-sphere interaction factor (520 and 760 min). (b) Fitting parameters obtained by fitting analysis: aggregate radius of gyration  $R_g$  (triangles in log-linear scale) and fractal dimension  $d_f$  (circles).

flexible rods when the mean aggregation number is not too high, as in our case ( $n = R_{90}/(kcM_{TE}) \leq 50$ ).<sup>9</sup>

In order to be able to detect larger aggregated species, up to dimensions on the order of micrometers, small-angle light scattering at  $q = 0.42 \mu\text{m}^{-1}$  was monitored during incubation at  $T = 37^\circ\text{C}$ , of ConA solutions at pH 8.9, at three different protein concentrations (0.12, 0.55, and 0.86 mg/mL). The time course of the small-angle static light scattered at the three different concentrations is reported in Figure 5. In the inset of Figure 5 the two sets of data corresponding to the higher concentrations are scaled to the third one ( $c_0 = 0.12 \text{ mg/mL}$ ),

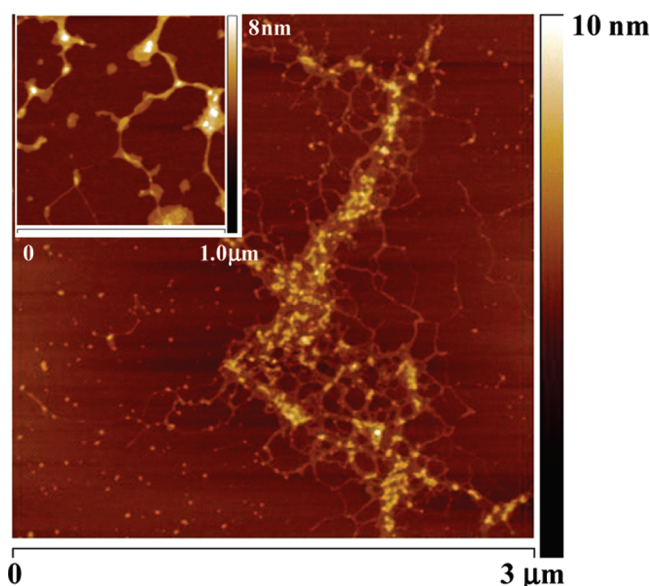


**Figure 7.** Tapping mode AFM image (height data) of ConA aggregates formed at pH 8.9 from 0.5 mg/mL sample after 400 min at  $37^\circ\text{C}$ , scan size  $3 \mu\text{m}$ . Long and simple fibrils are present, and those structures appear organized in a netlike way. The inset, scan size  $1 \mu\text{m}$ , shows a detail of another area of the same sample.

by the transformation  $t' = t(c/c_0)$ . Interestingly, a good overlap is obtained, indicating that the process of formation of large aggregates is the same at the different concentrations studied. The continuous line shown in the inset represents an exponential growth according to the expression  $I = I_0(1 + e^{t'/\tau_{\text{SALS}}})$  with  $\tau_{\text{SALS}} = 2343 \text{ min}$  (for  $c = c_0$ ).

In order to gain information on the structure of the aggregates during the process, Figure 6a reports some snapshots of the time evolution of the Rayleigh ratio as function of  $q$ , for the intermediate concentration (0.55 mg/mL). To carry on this experiment, twin solutions coming from the same sample have been monitored simultaneously in the LALS and SALS instruments. LALS and SALS data measured simultaneously provide information on aggregates size and structure over an extremely broad region of  $q$  ( $0.1 < q < 30 \mu\text{m}^{-1}$ ). In the early stages of the aggregation ( $t < 150 \text{ min}$  and  $qR_g < 1$ ), data can be analyzed with a Guinier model. Afterward, data can be well fitted by using a fractal model, according to the expression reported in the Experimental Methods section (eq 6). The continuous lines in Figure 6a represent the data-fitting curves. The best fits were obtained setting the fractal building unit radius  $r_0 = 5 \text{ nm}$  (see eq 6), compatible with the native protein size. We wish to note that changing this parameter up to 10 nm does not affect the fitting quality and yields a variation of the order of 2% in the other fitting parameters. Eventually, data corresponding to the fast increase of the SALS signal (Figure 5,  $c = 0.55 \text{ mg/mL}$ ,  $t > 500 \text{ min}$ ) were analyzed by adding also an interaction factor in the expression, mimicking a more complicated system. Figure 6b reports on the fitting parameters coming from the combined analysis. The radius of gyration was obtained directly from the Guinier analysis ( $t < 150 \text{ min}$ ) or by using the relation  $R_g = \{[(3d_f)/2]\xi\}^{1/2}$  from the cluster size  $\xi$  and the fractal dimension  $d_f$  ( $t > 150 \text{ min}$ ).<sup>12</sup>

The increase in the fractal dimension suggests a progressive thickening of the aggregates. The analysis with an additional

interaction term, modeled as hard-sphere interaction, gives a volume fraction of the interacting aggregates of about 0.13 in both cases, and a hard-sphere radius of about 2.5  $\mu\text{m}$ .

Figure 7 reports the AFM images of ConA aggregates formed in solution (0.5 mg/mL) after 400 min of incubation at  $T = 37^\circ\text{C}$ . Analogous results were found for the lower concentration after 20 h of incubation, in agreement with SALS results. Long and thin fibrils are present in the sample; these fibrils are organized in a netlike way (see inset). The thin fibrils' height is homogeneous in each region of the image and is about 3 nm. This value is comparable to the one previously measured after a shorter incubation time.<sup>23</sup> AFM measurements reported in Vetri et al.<sup>23</sup> gave a height distribution for the ConA tetramer of  $1.65 \pm 0.05$  nm. Such a low height for thin fibril is not surprising, since the interaction of the aggregate protein with mica in dehydrated conditions may reduce the measured size of ConA with respect to the size measured in fully hydrated conditions.<sup>35</sup>

As is evident, tangles formed by thicker and larger structures are superimposed over the thin fibrils; the width of these aggregates is heterogeneous all over the sample and varies in the range 30–250 nm, and their height also varies between 3 and 10 nm. Also for larger aggregates, the drying of the sample and the interaction with mica may reduce the measured height. However, the size and the spatial distribution of aggregates with different morphologies and shape are compatible with what is observed in solution through LALS and SALS measurements reported in Figures 5 and 6.

Overall, the data seem to indicate that the aggregation process develops in several and possibly intertwined stages. Different mechanisms occur on the same time scale and can be distinguished by the parallel use of different technique. In detail, ThT fluorescence signal increases only in the first part of the process, reaching a plateau in about 100 min, in connection with the elongation of thin fibrils.<sup>23</sup> These structures, characterized by intermolecular  $\beta$ -sheets<sup>34</sup> with strong H-bonding typical of amyloid fibrils,<sup>33</sup> are likely to orderly interact to form complex supramolecular assemblies. Indeed, after the first 100 min LALS signal keeps increasing, with a concentration dependent slope, reaching a plateau (see Figure 2) in longer time scale. Further association and supramolecular rearrangement still go ahead with formation of large aggregates up to dimensions of micrometers, as detected by dynamic light scattering and small-angle light scattering. Comparison of the time scale in the light-scattering experiments reported in Figures 2 and 5 shows that when LALS stops to increase (for  $c = 0.86$  mg/mL at about 200 min), SALS starts to rise, indicating that actually aggregation goes ahead until precipitation appears.

## DISCUSSION

**$\beta$ -Aggregate Structure Formation and Fibrils Growth.** The results obtained from light-scattering and ThT emission data suggest that these two methods are yielding complementary information on the processes going on. The time behavior of ThT data is significantly different from the one relative to light scattering. ThT data display indeed concentration-independent rate constants and reach saturation very soon with respect to light-scattering data, which on the contrary display a concentration dependence of rate constants and evolve for much longer times. The concentration independence in ThT data implies that the time behavior of the ThT signal is essentially brought about by conformational changes underlying the formation of  $\beta$ -

aggregate structures, and not simply by the association process. Two different models can explain the time behavior of ThT signal. In the first model, a conformational change is the rate-limiting step for the formation of small ThT-binding  $\beta$ -aggregate structures. In this scenario, the collision rate of the aggregating units must be faster than the conformational change rate, at all the explored concentrations, otherwise concentration-dependent ThT rate constants would be observed. In the second model, the relevant conformational change leads to some kind of non-native, aggregation-prone, tetramer, which is able to bind ThT. This hypothesis does not follow the paradigm of ThT fluorescence signal as a measure of fibril formation. On the other hand, there are few cases reported in the literature not following this paradigm (see, e.g., ref 36 on ThT binding to AchE).

Our experimental evidence is not sufficient to clearly distinguish between these two hypotheses. However, the first interpretation agrees with the most common attribution of the ThT signal to formation of intermolecular  $\beta$ -aggregate structures. Furthermore, the first hypothesis agrees also with the fact that in correspondence with the increase in ThT binding both the weight-averaged molecular mass  $\langle M_w \rangle$  and the  $z$ -averaged hydrodynamic radius  $R_h$  increases, prompting that an association is simultaneously undergoing.

This agrees also with the AFM data already published<sup>23</sup> that showed the formation of amyloid fibrils during the early stage of the aggregation. In the same paper, the conformational changes detected by ThT binding enhancement are correlated with an increase of  $\beta$ -aggregate structures as can be seen by comparison of fluorescence data with CD data.<sup>23</sup>

At the lowest concentration studied, the Rayleigh ratio can be fitted by using the expression

$$\frac{R_{90}}{kcM_w^0} = \frac{M_w}{M_w^0} = \left[ 1 + \frac{t}{zt_0} \right]^z \quad (7)$$

which describes a coagulation process.<sup>9</sup> Data fit parameters are  $z = 0.77$  and  $t_0 = 3.4$  min. The curve is shown in Figure 2b. In a colloidal aggregation framework, the function 7 is obtained by solving the Smoluchowsky equation, assuming a homogeneous kernel ( $k_{ai,aj} = a^\lambda k_{ij}$ , for all  $a$  values).  $k_{ai,aj}$  is the probability of association for clusters with aggregation number  $ai$  and  $aj$ , respectively, and  $k_{ij}$  represents the probability of association for clusters composed by  $i$  and  $j$  units, respectively.<sup>9</sup> The parameter  $z$  is related to the exponent  $\lambda$ , according to  $\lambda = (z - 1)/z$ . The  $z$  value obtained by the analysis leads to  $\lambda = -0.35$ , suggesting a mechanism of aggregation which is governed mainly by clusters diffusion. A fit of the highest concentration data according to the expression 7 in the region where there is no form factor contribution ( $t < 50$  min) would give  $z = 2.8$  and therefore  $\lambda = 0.64$  (about 2/3) (Figure 2b). This result indicates, unlike the low-concentration case, that at high concentration larger clusters have a higher probability to stick together than the small ones, thus suggesting that the aggregation mechanism is mainly driven by the formation of the aggregates exposed surface. On the other hand, time course SALS results highlight a heterogeneous aggregation mechanism that likely onsets quite early at the higher concentrations.

By scaling the time axis for the concentration, as in the inset of Figure 2b, it can be clearly seen that high-concentration samples lag behind during the early stage of the kinetics. This suggests that the formation of  $\beta$ -aggregate structures monitored by ThT increase is a concentration-independent rate-limiting step for the aggregation process.



The observed aggregation process occurs at pH 8.9, i.e., far from the isoelectric point of the protein (pH  $\sim$  5). In dilute conditions, electrostatic repulsion is likely to reduce the probability of casual collisions, which may lead to disordered assembly, so that the aggregation process requires more specific interactions, like those occurring in the formation of  $\beta$ -aggregates that are stabilized also by hydrophobic interactions.<sup>23</sup> The formation of these structures from destabilized molecules requires protein structure changes that are concentration independent. Once concentration increases, the formation of reactive  $\beta$ -structures may become a rate-limiting step.

The two concentrations studied are not extreme conditions, but the different regimes in these two cases are an indication of the connection and competition between the rate-limiting step formation of  $\beta$ -aggregates structure and the cluster–cluster condensation process onset. At the intermediate concentrations, the exponent  $z$  increases, crossing at  $c = 0.28$  mg/mL the condition where  $\lambda = 0$ , that is  $z = 1$ , meaning a classical mass-independent kernel, determined by a balance between the rates of the two processes. Notwithstanding the apparent complexity, all the intensity data at  $q = 23 \mu\text{m}^{-1}$  plotted as a function of the corresponding average hydrodynamic radius overlap. The line plotted in Figure 4 has a slope 2. A similar result has been discussed in a light-scattering study on the early aggregation of the A $\beta$ -peptide at low pH, where the agreement with the model of flexible rods is reported.<sup>9</sup> This similarity supports the interpretation that the aggregates detected in the first stage of ConA aggregation process, characterized by a mean aggregation number  $n = R_{90}/(kcM_{Tc}) \leq 50$  and a form factor close to 1, are mainly composed of fibrils at all the concentrations studied, as demonstrated by AFM measurements for a particular concentration in Vetri et al.<sup>23</sup>

**Aggregates Condensation and Structural Properties.** The combination of the small- and large-angle light scattering leads to a deeper comprehension of the aggregation process because, as it can be observed in Figure 5, the supramolecular assembly that apparently concludes, as seen by LALS, actually continues as monitored by SALS. Interestingly, as shown in the inset of Figure 5, small-angle light-scattering data at the three concentrations studied can be overlapped by scaling the time axis with the concentration. This result states that such kinetic process is the same at all the concentrations unlike the early step of the coagulation process. The scattered intensity rises exponentially, suggesting a mechanism similar to a heterogeneous nucleation, where the formation of such large aggregates is enhanced and maintained by the exposed surface of the same aggregates.<sup>37,38</sup>

The process is slowed down at some point by aggregates precipitation.

The combination of small- and large-angle light scattering again can give some more information on the structural properties of aggregates present in solution. The fractal model applied to the structure factor shows an increase of the fractal dimension, meaning a compaction of the aggregates followed by an increase of the aggregates average size. By imaging the aggregates with AFM, it is evident that large aggregates are present in solution. These are composed by a net of thin fibrils whose formation can be ascribed to the early step aggregation. The growth of tangles in such a net can explain the increase of the fractal dimension. At different times, similar aggregates are observed at low and high concentrations. It is worth noticing that after about 2 h of aggregation, the fractal dimension coming from MALS analysis is 1.7 (Figure 6b), while the exponent  $\alpha$  obtained by fitting

Rayleigh ratio vs hydrodynamic radius data is 2 (Figure 4). In this latter case, indeed the scaling relation reflects not only geometrical (size and shape) but also diffusional properties of the aggregates. The same result has been reported for the case of self-avoiding random polymers<sup>39</sup> and the early amyloid aggregation of the A $\beta$ -peptide at low pH.<sup>9</sup>

## CONCLUSIONS

This study on ConA aggregation makes it evident how important is the application of complementary experimental techniques to investigate protein aggregation processes. Indeed, the analysis of the data independently obtained by the different techniques allowed us to evidence multiple and interconnected mechanisms in ConA aggregation. This work reports that ConA, under the conditions here studied, presents: (1) a non-nucleated formation of fibril-like structures, stabilized by structural reorganization leading to an increase of intermolecular  $\beta$ -structures; (2) elongation of amyloid fibrils; and (3) supramolecular aggregation, with growth of compact aggregates.

The formation of intermolecular  $\beta$ -sheets appears to be the rate-limiting step of the fibrils formation process, according to the fact that the growth rate of ThT binding sites in the fibrillar aggregates in the first part of the process does not depend on protein concentration. Formation of the fibrillar aggregates may alter protein–solvent and protein–protein interactions, thus leading to the onset of a new aggregation pathway, describable as a cluster–cluster condensation process. This further supramolecular assembling is instead concentration dependent and, in the early stage of the aggregation process, it appears intertwined with the initial fibril formation process. Moreover, while cluster–cluster condensation strongly affects the light-scattering signal (sensitive to the aggregate mass), it does not contribute consistently to the formation of new binding sites for ThT molecules.

## ACKNOWLEDGMENT

We thank Dr. M. Manno for helpful discussion on the theoretical interpretation of data, and Dr. P. L. San Biagio and D. Bulone for their scientific support.

## REFERENCES

- (1) Selkoe, D. J. Folding proteins in fatal ways. *Nature* **2003**, 426 (6968), 900–904.
- (2) Nilsson, M. R. Techniques to study amyloid fibril formation in vitro. *Methods* **2004**, 34 (1), 151–160.
- (3) Dobson, C. Protein folding and misfolding. *Nature* **2003**, 426 (6968), 884–90.
- (4) Booth, D.; Sunde, M.; Bellotti, V.; Robinson, C.; Hutchinson, W.; Fraser, P.; Hawkins, P.; Dobson, C.; Radford, S.; Blake, C.; Pepys, M. Instability, unfolding and aggregation of human lysozyme variants underlying amyloid fibrillogenesis. *Nature* **1997**, 385 (6619), 787–93.
- (5) Valente, J.; Verma, K.; Manning, M.; Wilson, W.; Henry, C. Second virial coefficient studies of cosolvent-induced protein self-interaction. *Biophys. J.* **2005**, 89 (6), 4211–8.
- (6) Chiti, F.; Webster, P.; Taddei, N.; Clark, A.; Stefani, M.; Ramponi, G.; Dobson, C. Designing conditions for in vitro formation of amyloid protofilaments and fibrils. *Proc. Natl. Acad. Sci. U.S.A.* **1999**, 96 (7), 3590–4.
- (7) Makin, O.; Serpell, L. Structures for amyloid fibrils. *FEBS J.* **2005**, 272 (23), 5950–61.
- (8) Uversky, V. Intrinsic disorder in proteins associated with neurodegenerative diseases. *Front. Biosci.* **2009**, 14, 5188–238.

- (9) Carrotta, R.; Manno, M.; Bulone, D.; Martorana, V.; Biagio, P. L. S. Protofibril Formation of Amyloid  $\beta$ -Protein at Low pH via a Non-cooperative Elongation Mechanism. *J. Biol. Chem.* **2005**, *280* (34), 30001–30008.
- (10) Rosenbaum, D.; Zamora, P.; Zukoski, C. Phase behavior of small attractive colloidal particles. *Phys. Rev. Lett.* **1996**, *76* (1), 150–153.
- (11) McManus, J.; Lomakin, A.; Ogun, O.; Pande, A.; Basan, M.; Pande, J.; Benedek, G. Altered phase diagram due to a single point mutation in human gammaD-Crystallin. *Proc. Natl. Acad. Sci. U.S.A.* **2007**, *104* (43), 16856–61.
- (12) Brown, W. *Light Scattering, Principles and Development*; Oxford University Press: London, 1996.
- (13) Zhang, Y.-H.; Leliveld, S. R.; Kooistra, K.; Molenaar, C.; Rohn, J. L.; Tanke, H. J.; Abrahams, J. P.; Noteborn, M. H. M. Recombinant apoptin multimers kill tumor cells but are nontoxic and epitope-shielded in a normal-cell-specific fashion. *Exp. Cell Res.* **2003**, *289* (1), 36–46.
- (14) Carrotta, R.; Di Carlo, M.; Manno, M.; Montana, G.; Picone, P.; Romancino, D.; San Biagio, P. L. Toxicity of recombinant  $\{\beta\}$ -amyloid prefibrillar oligomers on the morphogenesis of the sea urchin *Paracentrotus lividus*. *FASEB J.* **2006**, *20* (11), 1916–1917.
- (15) LeVine, H. Thioflavine t interaction with synthetic alzheimer's disease  $\beta$ -amyloid peptides: detection of amyloid aggregation in solution. *Protein Sci.* **1993**, *2*, 404–410.
- (16) Krebs, M. R. H.; Bromley, E. H. C.; Donald, A. M. The binding of thioflavin-T to amyloid fibrils: localisation and implications. *J. Struct. Biol.* **2005**, *149* (1), 30–37.
- (17) Groenning, M.; Olsen, L.; van de Weert, M.; Flink, J. M.; Frokjaer, S.; Jørgensen, F. S. Study on the binding of Thioflavin T to  $[\beta]$ -sheet-rich and non- $[\beta]$ -sheet cavities. *J. Struct. Biol.* **2007**, *158* (3), 358–369.
- (18) Foderà, V.; Librizzi, F.; Groenning, M.; van de Weert, M.; Leone, M. Secondary nucleation and accessible surface in insulin amyloid fibril formation. *J. Phys. Chem. B* **2008**, *112*, 3853–8.
- (19) Biancalana, M.; Koide, S. Molecular mechanism of Thioflavin T binding to amyloid fibrils. *BBA* **2010**, *1804*, 1405–1412.
- (20) Becker, J.; Reeke, G. J.; Wang, J.; Cunningham, B.; Edelman, G. The covalent and three-dimensional structure of concanavalin A. III. Structure of the monomer and its interactions with metals and saccharides. *J. Biol. Chem.* **1975**, *250* (4), 1513–24.
- (21) Wang, J.; Cunningham, B.; Waxdal, M.; Edelman, G. The covalent and three-dimensional structural of concanavalin A. I. Amino acid sequence of cyanogen bromide fragments F1 and F2. *J. Biol. Chem.* **1975**, *250* (4), 1490–502.
- (22) Emsley, J.; White, H. E.; O'Hara, B. P.; Oliva, G.; Srinivasan, N.; Tickle, I. J.; Blundell, T. L.; Pepys, M. B.; Wood, S. P. Structure of pentameric human serum amyloid P component. *Nature* **1994**, *367* (6461), 338–345.
- (23) Vetri, V.; Canale, C.; Relini, A.; Librizzi, F.; Militello, V.; Gliozzi, A.; Leone, M. Amyloid fibrils formation and amorphous aggregation in concanavalin A. *Biophys. Chem.* **2007**, *125* (1), 184–90.
- (24) Foderà, V.; Groenning, M.; Vetri, V.; Librizzi, F.; Spagnolo, S.; Cornett, C.; Olsen, L.; van de Weert, M.; Leone, M. Thioflavin T hydroxylation at basic pH and its effect on amyloid fibril detection. *J. Phys. Chem. B* **2008**, *112*, 15174–81.
- (25) Stepanek, P. In *Dynamic Light Scattering: The method and some applications*; Brown, W., Ed.; Clarendon Press: Oxford, UK, 1993.
- (26) Bulone, D.; Giacomazza, D.; Martorana, V.; Newman, J.; San Biagio, P. Ordering of agarose near the macroscopic gelation point. *Phys. Rev. E. Stat. Nonlin. Soft. Matter Phys.* **2004**, *69* (4 Pt 1), 041401.
- (27) Olson, M.; Liener, I. The association and dissociation of concanavalin A, the phytohemagglutinin of the jack bean. *Biochemistry* **1967**, *6*, 3801–8.
- (28) Pflumm, M.; Beychok, S. Alkali and urea induced conformation changes in concanavalin A. *Biochemistry* **1974**, *13*, 4982–7.
- (29) Kudou, M.; Shiraki, K.; Takagi, M. Characterization of heat-induced aggregates of concanavalin A using fluorescent probes. *Sci. Technol. Adv. Mater.* **2004**, *5* (3), 339–341.
- (30) Kudou, M.; Shiraki, K.; Takagi, M. Stretched-exponential analysis of heat-induced aggregation of apo-concanavalin A. *Protein J.* **2005**, *24* (3), 193–9.
- (31) Vetri, V.; Librizzi, F.; Militello, V.; Leone, M. Effects of succinylation on thermal induced amyloid formation in Concanavalin A. *Eur. Biophys. J.* **2007**, *36* (7), 733–41.
- (32) Carrotta, R.; Bauer, R.; Waninge, R.; Rischel, C. Conformational characterization of oligomeric intermediates and aggregates in  $\beta$ -lactoglobulin heat aggregation. *Protein Sci.* **2001**, *10* (7), 1312–8.
- (33) Vetri, V.; Carrotta, R.; Picone, P.; Di Carlo, M.; Militello, V.; Concanavalin A aggregation and toxicity on cell cultures. *Biochim. Biophys. Acta* **2009**.
- (34) Krebs, M.; Domike, K.; Cannon, D.; Donald, A. Common motifs in protein self-assembly. *Faraday Discuss.* **2008**, *139*, 265–74 discussion on pages 309–25, 419–20.
- (35) Jerzy Mielczarski, A.; Dong, J.; Mielczarski, E. Real Time Evaluation of Composition and Structure of Concanavalin A Adsorbed on a Polystyrene Surface. *J. Phys. Chem. B* **2008**, *112*, 5228–5237.
- (36) De Ferrari, G. V.; Mallenders, W. D.; Inestrosa, N. C.; Rosenberry, T. L. Thioflavin T is a fluorescent probe of acetylcholinesterase peripheral site that reveals conformational interactions between the peripheral and acylation sites. *J. Biol. Chem.* **2001**, *276* (26), 23282–23287.
- (37) Ferrone, F. Analysis of protein aggregation kinetics. *Methods Enzymol.* **1999**, *309*, 256–274.
- (38) Librizzi, F.; Rischel, C. The kinetic behavior of insulin fibrillation is determined by heterogeneous nucleation pathways. *Protein Sci.* **2005**, *14*, 3129–3134.
- (39) de Gennes, P.-G. *Scaling Concepts in Polymer Physics*; Cornell University Press: Ithaca, NY, 1979.